Heterogeneous & Homogeneous & Bio- & Nano-

CHEMCATCHEM

CATALYSIS

Accepted Article

Title: The key role of nanocasting in gold-based Fe2O3 nanocasted catalysts for oxygen activation at the metal-support interface

Authors: Tomás García, Jose Manuel López, Benjamín Solsona, Rut Sanchis, David J Willock, Thomas Davies, Li Lu, Qian He, Christopher J Kiely, and Stuart H. Taylor

To be cited as: *ChemCatChem* 10.1002/cctc.201900210

Link to VoR: http://dx.doi.org/10.1002/cctc.201900210

A Journal of

ChemPubSoc Europe

WILEY-VCH

www.chemcatchem.org

WILEY-VCH

FULL PAPER

The key role of nanocasting in gold-based Fe_2O_3 nanocasted catalysts for oxygen activation at the metal-support interface

Tomás García,*[a] José M. López,[a] Benjamín Solsona,*[b] Rut Sanchis,[b] David J. Willock,[c] Thomas E. Davies,[c] Li Lu,[d] Qian He,[c] Christopher J. Kiely,[c,d] and Stuart H. Taylor*[c]

Abstract: The total oxidation of propane, a representative Volatile Organic Compound, has been studied using gold-based α-Fe_2O_3 catalysts. Catalysts consisting of gold nanoparticles confined in nanostructured Fe_2O_3 prepared by a nanocasting route present the highest catalytic activity for propane total oxidation, and the activity is significantly greater than those of gold-based catalysts where iron oxide supports are prepared by other conventional methods, such as calcination. Detailed characterization and Density-functional theory (DFT) studies have been undertaken in order to explain the enhancement in catalytic properties. The presence of confined gold nanoparticles on the nanocast Fe_2O_3 facilitates the production of highly reactive oxygen vacancies at the metal-support interface, increasing the catalyst performance. Both the development of a microporous/mesoporous structure in the iron oxide support and the presence of a mixed surface phase of Si and Fe oxides, seem to be key parameters, being both features inherent in the nanocasting process from silica templates. Additionally, the catalytic activity is enhanced due to other positive effects, which are closely related to the nanocasting preparation method: i) a higher contact surface area between partially confined small gold nanoparticles in the internal mesoporosity of the nanostructured support and the metal oxide and; ii) a more reducible support due to the presence of more active surface lattice oxygen.

Introduction

Most of the efficient catalysts for the total oxidation of volatile organic compounds are based on noble metals, primarily palladium and platinum. However, gold is scarcely used in industrial VOC catalyst formulations, due to its lower reactivity and lower stability at high reaction temperatures. Interestingly, research undertaken for the past 5-10 years has led researchers to re-consider the possible contribution of Au nanoparticles in catalysts for VOC emission control by oxidation.[1],[2] This has been driven by new developments in catalyst design, and by the greater availability of gold compared to platinum and palladium.

For gold catalysts, the oxidation state has been reported to be a key factor in VOC oxidation activity, although there is a surprising lack of agreement on precise details from studies in the literature. From a number of reports cationic gold is assumed to be the active site,[3], [4] whereas others propose that metallic gold is more reactive than $Au^{\delta+}$ species.[5]-[7] In several studies, the co-existence of $Au^{\delta+}$ and Au^0 has been postulated as the most active combination;[8]-[10] with metallic gold involved in the adsorption and activation of the organic compound, whilst the excess oxygen associated with cationic gold participates in oxygen activation. A positive feature of adding gold is to improve the redox properties of metal oxides, leading to an enhanced reactivity compared to the support alone. However, in order to achieve satisfactory results, the preparation method and the nature of the support have to be controlled appropriately.

The characteristics of gold catalysts differ significantly to those of Pt and Pd, as it appears that the role of the support is much more important for gold catalysts.[11],[12] The primary role of the metal oxide supports for Pt and Pd-based catalysts has been considered to be related to their capacity to impart the noble metal particles with the right crystallite size and oxidation state.[13] In contrast for gold-based catalysts, the situation may be considerably more complex, with catalytic performance being dictated by both the properties of the support and the gold components, which often lead to activity enhancements due to synergistic effects.[2] For instance, the high activity observed for Au/FeO_x catalysts in the oxidation of a series of VOCs has been related to the presence of highly dispersed gold. Small gold nanoparticles have been proposed to modify the characteristics of the iron oxide support by decreasing the strength of the Fe-O bonds, thus increasing the mobility of the lattice oxygen.[14] The presence of gold can also in principle distort the iron oxide lattice which may positively influence the catalytic performance.[15]

In the present work, iron oxide has been selected as a support for gold nanoparticles. Iron oxide, apart from being inexpensive, environmentally friendly and readily available, is conveniently synthesised, and it is also reasonably active for the total oxidation of VOCs including propane.[16]-[19] For bulk iron oxide catalysts, it has been observed that high surface area and reducibility of the iron species are the key parameters needed to achieve high catalytic activity. This is in accordance with the redox Mars-van Krevelen mechanism that controls the oxidation of propane on iron oxide. For supported iron oxide catalysts, the extent of iron oxide dispersion determines the catalytic activity. In particular, more highly dispersed iron oxide species have been reported to be more reducible than highly aggregated species, and consequently this leads to higher catalytic activity.[20]

For bulk oxide catalysts, the nano-architecture of the iron oxides does not seem to be of paramount importance for total

[a] Dr. T. García, Dr. J.M. López. Instituto de Carboquímica (CSIC), C/Miguel Luesma Castán 4, 50018 Zaragoza, Spain. E-mail: tomas@icb.csic.es
[b] Dr. B. Solsona, Dr. R. Sanchis. Departament d´Enginyeria Química, Universitat de València, C/ Dr. Moliner 50, 46100 Burjassot, Valencia, Spain. E-mail: benjamin.solsona@uv.es
[c] Dr. D.J. Willock, Dr. T.E. Davies, Dr. Q. He, Prof. C.J. Kiely, Prof. S.H. Taylor. Cardiff Catalysis Institute, School of Chemistry, Cardiff University, Main Building, Park Place, Cardiff, CF10 3AT, UK. E-mail: taylorsh@cardiff.ac.uk
[d] L. Lu, Prof. C.J. Kiely. Department of Materials Science and Engineering, Lehigh University, 5 East Packer Avenue, Bethlehem, PA 18015-3195, USA.

Supporting information for this article is given via a link at the end of the document.

oxidation of VOCs. Ordered mesoporous iron oxides can be highly active and stable, but do not seem to offer additional advantages when compared to other high surface area FeO_x materials.[18], [19]

Gold supported on nanostructured iron oxide has previously been prepared and tested as a catalyst for CO oxidation, and they show higher activities than other Au/FeO_x catalysts.[21] This improved performance, in addition to factors such as small particle size and high surface area, is also related to the presence of a large amount of hydroxylated iron species. In other work, it was reported that the catalytic activity for CO oxidation can be enhanced using nanostructured α-Fe_2O_3 with relatively small pores that are of suitable dimensions to accommodate gold nanoparticles inside.[22] The importance of accommodating particles into the pores has also been observed with other supported noble metal catalysts. For example, Pt deposited into microscale mesoporous CeO_2 presented higher activity for the oxidation of benzene, than when Pt was deposited onto ceria nanocubes.[23] This enhancement was proposed to be related to the formation of active interface sites between and the support. Following this line of reasoning, the present work investigates catalysts consisting of gold deposited on mesoporous Fe_2O_3 prepared by a nanocasting route for the total oxidation of propane, a representative VOC. These catalysts have been synthesized so that gold particles are partially confined within the mesopores of the nanostructured iron oxide. Our study probes how these restrained gold particles affect the surface of the iron oxide and the gold/support interface and consequently the catalytic performance. For comparative purposes, gold supported on both a non-mesoporous iron oxide and a mesoporous iron oxide prepared with oxalic acid as a swelling agent were also investigated.

Results and Discussion

Catalytic activity.

Gold-based Fe_2O_3 catalysts were tested for the total oxidation of propane. Conversion as a function of temperature is shown in Figure 1A for the catalysts based on the iron oxide prepared by a hard template nanocasting method. For comparison gold-free and gold containing iron oxides, in which the iron oxide has been prepared by other methods, have also been tested (Figures 1B, 1C and Table 1). For all catalysts the main reaction product was CO_2. In some cases, low selectivity to propylene was noted (but only at very low conversion) and propylene selectivity decreased rapidly as conversion increased.

The propylene yield never exceeded 1%. Carbon monoxide was not detected, but due to the detection limits of the GC thermal conductivity detector a very low selectivity to this product cannot be ruled out. Table 1 summarizes the catalytic reaction temperatures of T_{10}, T_{50} and T_{90} (corresponding to the temperature for 10, 50 and 90% propane conversion respectively).

The total propane oxidation activity of the supports alone has also been studied. In agreement with previously published data,[18] the mesoporous Fe_2O_3 support prepared by the nanocasting route (Fe_2O_3-HT) showed a light-off temperature slightly higher than nanocrystalline Fe_2O_3 supports, prepared by either the soft templating route (Fe_2O_3-SC) or by calcination of the iron(II) nitrate precursor (Fe_2O_3-C).

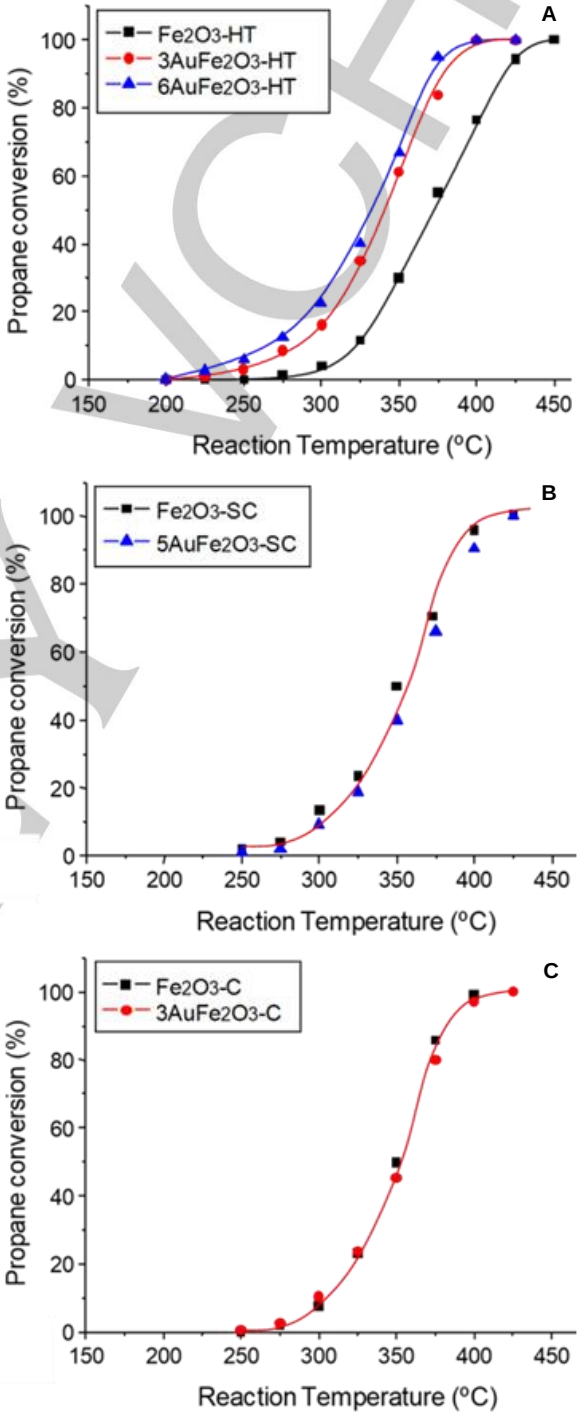

Figure 1. Propane conversion as a function of temperature over gold-free and gold-containing iron oxide catalysts. The supports have been prepared using A) hard template nanocasting method, B) soft chemistry method and C) simple calcination procedure. *Reaction conditions:* 8,000 vppm propane in air, GHSV = 100,000 h^{-1}.

Interestingly, it can be observed from Figure 1 that the efficacy of the catalytic combustion of propane over the corresponding gold-based Fe_2O_3 catalysts greatly depended on the support characteristics. Whilst both the $3AuFe_2O_3$-HT and $6AuFe_2O_3$-HT catalysts showed an enhanced activity compared with the parent Fe_2O_3-HT nanocast support, a similar positive effect was not observed for either the gold-based Fe_2O_3-C catalyst or the gold-based Fe_2O_3-SC catalyst. The mass normalised order of activity followed the sequence:

$6AuFe_2O_3$-HT > $3AuFe_2O_3$-HT > Fe_2O_3-SC > Fe_2O_3-C ≈ $3AuFe_2O_3$-C > $5AuFe_2O_3$-SC > Fe_2O_3-HT.

Table 1. Summary of catalytic activity for the various Au/Fe_2O_3-HT catalysts expressed as the temperature for 10, 50 and 90% propane conversion to CO_2 (T_{10}, T_{50} and T_{90}), and mass normalised rates of propane oxidation

	Propane oxidation[a]			
	T_{10} / °C	T_{50} / °C	T_{90} / °C	Catalytic activity[b]
Fe_2O_3-C	300	350	385	71
$3AuFe_2O_3$-C	305	355	400	90
Fe_2O_3-SC	295	350	385	107
$5AuFe_2O_3$-SC	300	355	385	81
Fe_2O_3-HT	317	370	418	34
$3AuFe_2O_3$-HT	279	339	387	146
$6AuFe_2O_3$-HT	268	334	370	198

[a] Reaction conditions: 8000 vppm propane in air, GHSV = 100,000 h^{-1}. [b] Catalyst activity determined at 300 °C and expressed in $g_{propane}\ kg_{cat}^{-1}\ h^{-1}$.

Notably, the T_{10} and T_{50} values decreased from 317 °C to 268 °C and from 370 °C to 334 °C, respectively, after deposition of 6 wt% gold onto the Fe_2O_3-HT support prepared by a nanocasting route. The stability of the most active catalyst for the propane total oxidation, $6AuFe_2O_3$-HT, was also assessed. It can be observed that this catalyst was not only showing an outstanding stability with the time on line experiment but also during cyclic operation (see Figure 2).

Catalyst characterisation.

The gold loadings for different gold-based Fe_2O_3 catalysts were measured by XEDS analysis and experimental values are reported in Table 2. It was observed that measured gold loadings were in good agreement with the expected nominal values, implying that most of the gold precursor was successfully deposited on the catalyst support. Nitrogen adsorption isotherms are presented in Figure 3A for the catalysts prepared on the hard and soft templated iron oxide supports. The isotherms confirmed the mesoporous character of the solid support prepared by the nanocasting route (denoted as Fe_2O_3-HT). The nanostructured support showed a markedly high specific surface area of 185 $m^2\ g^{-1}$, with a total pore volume of 0.49 $cm^3\ g^{-1}$. The BJH method applied to the adsorption branch of the isotherm (see Figure 3C), showed a broad mesopore size distribution centred at 18 nm. KIT-6 consists of two interpenetrating mesoporous channels linked by microporous channels.[24], [25]

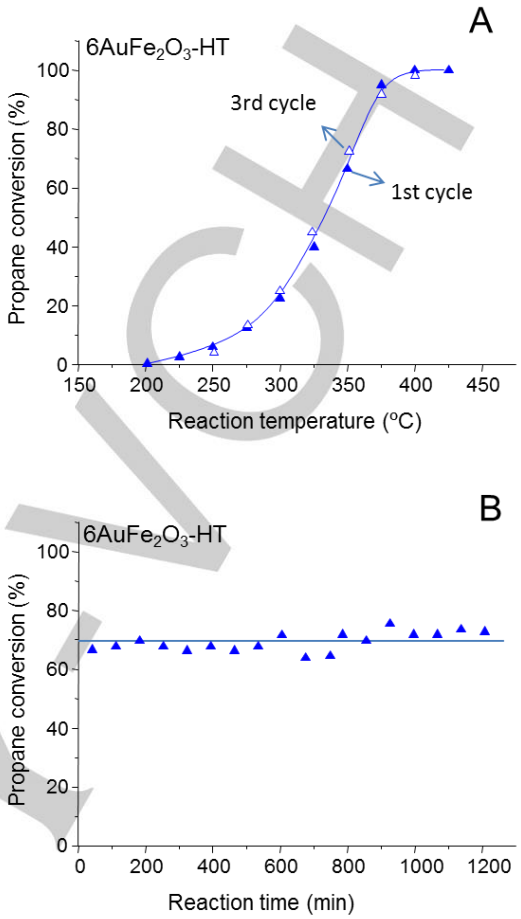

Figure 2. Propane conversion for the $6AuFe_2O_3$-HT catalyst as a function of the A) reaction temperature during cyclic operation; B) time on line. *Reaction conditions:* 8,000 vppm propane in air, GHSV = 100,000 h^{-1}, temperature = 350 °C.

During the nanocasting process, the KIT-6 mesochannels and their connecting microchannels are filled and then the silica wall material between them is etched away, generating pores of approximately 4 nm in dimension. However, varying the hydrothermal conditions during the KIT-6 synthesis can lead to a lower proportion of KIT-6 microchannels. Consequently, the simultaneous occupation of the KIT-6 microchannels is not fully achieved and a broad mesopore size distribution centred at 18 nm is obtained,[25] which is consistent with observations in the current study. Additionally, it is worth noting that for the Fe_2O_3-HT support there is also some evidence of macropore formation, arising from larger interstitial pores created between the hard-template particles. The presence of this macroporosity could be beneficial, as it can potentially improve the diffusion of the gold nanoparticle precursor into the inner porosity during the deposition-precipitation preparation process. After loading gold nanoparticles, at 3 wt. % and 6 wt. %, onto the Fe_2O_3-HT support, the BET surface area decreased slightly to 173 $m^2\ g^{-1}$ and 177 $m^2\ g^{-1}$, respectively, whilst total pore volume decreased more significantly from 0.49 $cm^3\ g^{-1}$ to 0.38 $cm^3\ g^{-1}$ and 0.37 $cm^3\ g^{-1}$ respectively. These observations can be linked to the partial blocking of the large mesopores on the Fe_2O_3 support by Au

nanoparticles. Accordingly, BJH pore size distributions of the gold-based Fe_2O_3-HT catalysts showed that the maxima of the distribution decreased from 18 to 12 nm after Au deposition (Figure 3C).

Table 2. Textural parameters of the KIT-6 silica template and hard templated Fe_2O_3 supports and the corresponding gold containing catalysts.

	[Au][a] / wt %	S_{BET}[b] / $m^2 \cdot g^{-1}$	V_T[c] / $cm^3 \cdot g^{-1}$	d_0[d] / nm
KIT-6	-	809	0.94	5.5
Fe_2O_3-C	-	24	0.05	47
3AuFe$_2$O$_3$-C	2.9	28	0.04	46
Fe_2O_3-SC	-	82	0.42	21
5AuFe$_2$O$_3$-SC	4.1	60	0.44	28
Fe_2O_3-HT	-	185	0.49	12
3AuFe$_2$O$_3$-HT	2.6	173	0.38	8.4
6AuFe$_2$O$_3$-HT	4.9	177	0.37	9.1

[a] Percentage of gold determined by XEDS. [b] Specific surface area deduced from the isotherm analysis in the relative pressure range of 0.05-0.25. [c] Total pore volume at relative pressures 0.95. [d] average pore diameter calculated from the adsorption branch of the isotherm using the BJH method.

Additionally, the BJH distribution revealed that there was a loss of the macroporosity originally available for the bare Fe_2O_3-HT support. In agreement with this, TEM analysis (presented later in Figure 5), shows that ordered interstitial gaps that make up much of the macroporosity were mostly missing from the gold-based Fe_2O_3-HT catalysts as compared to the bare support. As a result, the preparation method creates gold particles that are partially confined by the internal mesoporosity of the Fe_2O_3-HT support, which, in turn, may increase the metal-support contact area compared to gold nanoparticles supported on the external surface of the more conventional metal oxide support. This hypothesis was further confirmed by non-local density functional theory (NL-DFT) analysis of the adsorption isotherm branch (Figure 3B). Interestingly, NL-DFT pore size distributions clearly showed the existence of some microporosity in the Fe_2O_3-HT sample, with a narrow peak centered at 1.4 nm. Furthermore, this peak, which had almost disappeared after 3 wt. % gold was added, was completely absent after 6 wt. % gold addition. Therefore, it is possible that micropores intersecting the Fe_2O_3-HT surface could act as anchoring points for small gold nanoparticles. It should also be pointed out that the NL-DFT model could accurately reproduce the N_2 adsorption isotherm data, which strongly supports the proposed model. The mesoporous support formed by aggregation of nanoparticles (Fe_2O_3-SC) showed lower specific surface area than the nanostructured support (Fe_2O_3-HT), at 82 and 185 $m^2 g^{-1}$ respectively, but only a slightly lower total pore volume, at 0.42 and 0.49 $cm^3 g^{-1}$ respectively (Table 2). Comparing both isotherms (Figure 3A) it can be observed that the increase in slope at low partial pressures (*ca.* 0.4), typical of mesoporous materials with intra-particle pore systems, is more noticeable for the nanostructured support, whilst the Fe_2O_3-SC sample presents a more visible increase of the slope at higher relative pressures, indicating a more substantial contribution from inter-particle porosity.

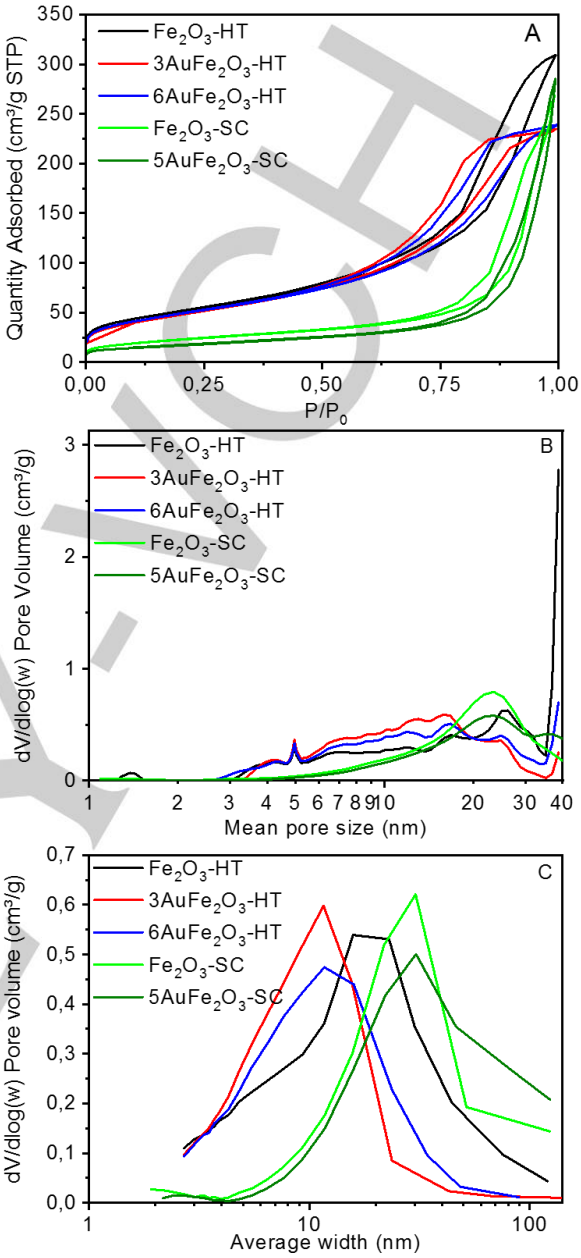

Figure 3. (A). N_2 adsorption isotherm data, (B). NL-DFT pore size distribution and (C) BJH pore size distribution for the various gold-free and gold-containing Fe_2O_3 catalysts prepared by hard and soft templating methods.

Accordingly, the pore size distribution of this sample is shifted to higher values and centered at about 30 nm (Figure 3C), with an average pore dimension of 21 nm compared with the 12 nm presented in the 3D network nanostructured support. After loading gold nanoparticles at 5 wt.% onto the Fe_2O_3-SC support, the BET surface area decreased significantly to 60 $m^2 g^{-1}$, whilst the total pore volume remained at a comparable value of 0.44 $cm^3 g^{-1}$. This behavior can be linked to the deposition of gold nanoparticles onto the mesoporous external surface of the Fe_2O_3-SC nanoparticles, as shown in Figure 3. In line with this, it should

be noted that the NL-DFT model did not show any features related to the presence of microporosity in the Fe_2O_3-SC sample, as was observed for the nanostructured Fe_2O_3-HT support. In direct contrast, N_2 adsorption analysis of the catalyst derived from the iron(II) nitrate salt revealed a low porosity with a specific surface area of 22 $m^2 g^{-1}$ (Table 2). A comparable value of 28 $m^2 g^{-1}$ was obtained after 3 wt% gold deposition, indicating that gold nanoparticles have been deposited exclusively on the external surface of the support.

Powder X-ray diffraction (XRD) was used to identify the crystalline phases present in the different materials. Figure 4 shows the XRD patterns of the iron oxide obtained by the hard-templating route (Fe_2O_3-HT) and the corresponding iron-oxide-supported Au catalysts (3AuFe$_2$O$_3$-HT and 6AuFe$_2$O$_3$-HT). These samples only showed two tiny broad peaks at 2θ = 33.2° and 35.7°, which could be tentatively indexed to 104 and 110 reflections from α-Fe_2O_3.[26] On the other hand, both nanocrystalline iron oxide supports (Fe_2O_3-SC and Fe_2O_3-C), and those catalysts with Au supported on them (5AuFe$_2$O$_3$-SC and 3AuFe$_2$O$_3$-C) showed nine diffraction peaks corresponding to reflections indexed to rhombohedral α-Fe_2O_3.[26] A smaller mean iron oxide crystallite size was obtained for the Fe_2O_3-SC support compared with the

Fe_2O_3-C counterpart, (*i.e.,* 12 nm and 24 nm respectively). Furthermore, the deposition of gold nanoparticles onto these supports did not significantly change the mean crystallite sizes. Moreover, none of the gold-loaded catalysts, irrespective of the support, exhibited peaks corresponding to reflections from gold, which indicates the presence of highly dispersed gold nanoparticles. Low angle XRD patterns (Figure S1) showed a mesoporous structure for the Fe_2O_3-HT sample with a decrease in the intensity after gold deposition and with no evidence of crystalline order. These result matches with the TEM observations presented below.

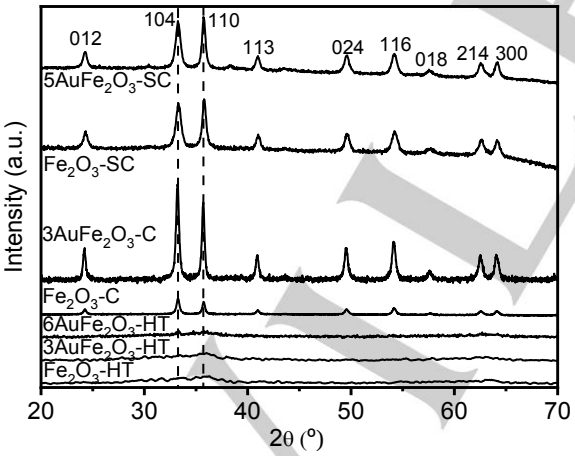

Figure 4. Wide angle XRD patterns of the catalysts obtained by hard templating (Fe_2O_3-HT, 3AuFe$_2$O$_3$-HT and 6AuFe$_2$O$_3$-HT), soft templating (Fe_2O_3-SC and 5AuFe$_2$O$_3$-SC) and those derived by precipitation from a nitrate salt precursor (Fe_2O_3-C and 3AuFe$_2$O$_3$-C).

Figure 5 shows representative bright field (BF) TEM micrographs of the Fe_2O_3-HT and Fe_2O_3-C samples. From Figure 5 (a), it can be observed that the Fe_2O_3-HT support presents a well-ordered structure, in accordance with it being an inverse replica of the KIT-6 template, composed of uniform nanoparticles linked by nanocrystalline bridges. The average primary particle size in the Fe_2O_3-HT sample (determined from measurements on more than 200 particles) was found to be 7 ± 1 nm.

Previously published selected area electron diffraction data [19] confirmed the nanocast support and Fe_2O_3-C materials to have a Fe_2O_3 structure (JCPDS: 85-0599) with space group R-3c. After the incorporation of gold into the mesoporous iron oxide through deposition precipitation, the ordered structure derived from the template appears to be lost, as shown in Figure 5(b). Nevertheless, the iron oxide primary particle size remains small (~7 nm), as compared to the non-porous iron oxide sample (Figure 5(c)), which has a particle size distribution ranging from about 20 to 50 nm.

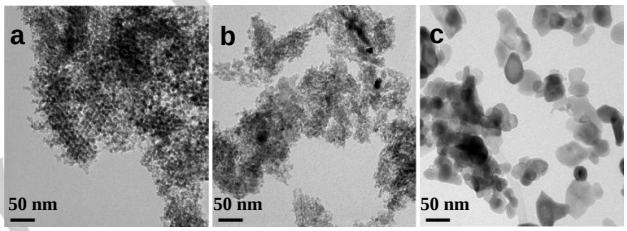

Figure 5. Representative bright field (BF) TEM images of (a) the Fe_2O_3-HT support material, (b) the 6AuFe$_2$O$_3$-HT catalyst and (c) the Fe_2O_3-C support material. Remnants of the ordered template network can be clearly seen in Fe_2O_3-HT material, but this has essentially collapsed after depositing Au, as shown in (b). The primary particle size of the iron oxide support in 6AuFe$_2$O$_3$-HT is significantly smaller than that of the conventional iron oxide support shown in (c).

The gold nanoparticles can be distinguished from the iron oxide support using atomic number (*Z*) contrast in a scanning transmission electron microscope (STEM) using the high angle annular dark field (HAADF) imaging mode. As shown in Figures 6(a-c), gold nanoparticles from 2 to 6 nm in size can be found in the 6AuFe$_2$O$_3$-HT sample. Occasionally larger particles of 20 nm can be also found (Figure S2). A comparable particle size distribution of Au particles, ranging mainly from 2 to 8 nm, and occasionally larger particles above 30-40 nm could be found in the 5Au Fe_2O_3-SC catalyst (Figure 7). Therefore, gold particle size does not seem to exert a key role in the better catalytic performance observed for gold catalyst supported on nanocasted iron oxide compared to the other iron oxide supports.

Interestingly, the iron oxide support material in the 6AuFe$_2$O$_3$-HT catalyst appears to have significant silicon oxide content at its surface. As shown in Figures 6(d-e), X-ray energy dispersive spectra (XEDS) acquired while the electron beam was scanning the area 1 (the near surface region) and area 2 (the bulk) of the iron oxide grain respectively. After normalising the two spectra using the total intensities of Fe K and Cu K peaks, a significant difference in the Si K peak intensities can be established. This suggests that the significant additional Si K signal arising from the near surface region (area 1) as compared to area 2 is not just from the internal fluorescence in the XEDS silicon drift detector, which is a common spectral artefact.

10.1002/cctc.201900210

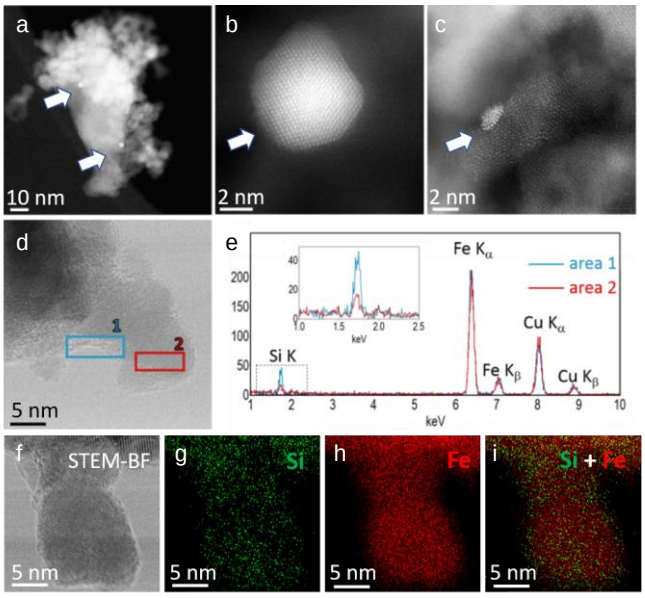

Figure 6. Representative STEM characterization results from the $6AuFe_2O_3$-HT catalyst. (a-c) High angle annular dark field (HAADF) *Z*-contrast micrographs of the catalysts showing Au nanoparticles ranging from 2-6 nm in size (indicated by white arrows). (d) Representative STEM bright field (BF) image of the iron oxide support material in the $6AuFe_2O_3$-HT catalyst and (e) the corresponding X-ray energy dispersive spectra (XEDS) acquired from the two regions indicated. The XEDS two spectra in (e) were normalised based on the intensities of the Fe K peaks and Cu K peaks (the latter of which originates from the TEM grid). (f) STEM-BF image and the corresponding XEDS maps of (g) Si and (h) Fe. (i) shows an overlay of the Si (green) and Fe (red) map.

This observation provides clear evidence of a genuine ultra-thin Si containing layer (most likely silicon dioxide) on the iron oxide support, which may originate from an incomplete etching away of the KIT-6 silica template. Qualitative XEDS mapping shown in Figure 6(f-i) suggested that the surface is likely to be a mixed phase of Si and Fe oxides.

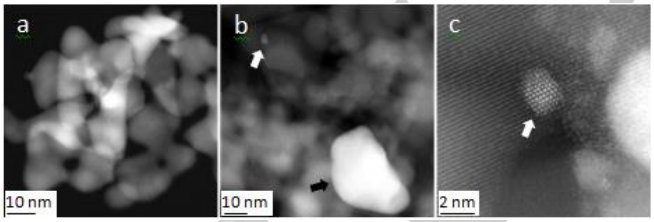

Figure 7. Representative STEM-HAADF micrographs from the $5AuFe_2O_3$-SC catalyst. (a) Micrograph showing the typical size and morphology of the iron oxide support grains (b) and (c) small Au nanoparticles about 2 nm in size (indicated by white arrows) as well as relatively large Au particles (black arrow) are clearly evident in the $5AuFe_2O_3$-SC catalyst.

The gold oxidation states for the $3AuFe_2O_3$-HT, $6AuFe_2O_3$-HT and $3AuFe_2O_3$-C catalysts were characterized using XPS by analysing the Au 4f spectra (Figure 8a). All the samples examined displayed peaks at the binding energies typical of metallic gold.[27]

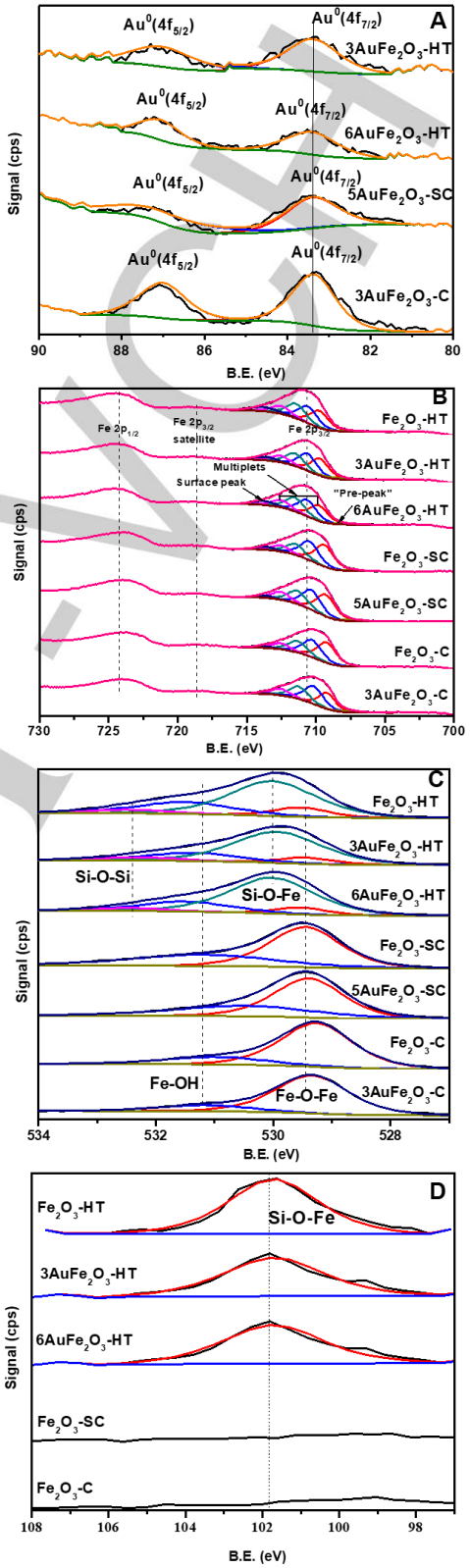

Figure 8. X-ray photoelectron spectra of various iron oxide supports and the corresponding gold loaded Fe_2O_3 catalysts. (A) Au 4f; (B) Fe 2p; (C) O 1s and (D) Si 2p spectra.

The oxidation state of the iron species was also characterized by XPS. The deconvolution of the Fe2p region was more challenging due to the presence of four peaks, corresponding to the $Fe2p_{3/2}$ multiplet (Figure 8b). All the materials examined presented the four peaks at binding energies that matched perfectly with those expected for the Fe^{3+} multiplet (*i.e.,* 709.8, 710.7, 711.4 and 712.3 eV), with no peaks at binding energies corresponding to Fe^{2+} species.[28] The results of these more surface sensitive analyses are in good agreement with bulk phase XRD analyses that revealed α -Fe_2O_3 as the unique crystalline phase. Somewhat surprisingly, the O 1s spectra clearly showed different features when comparing the mesoporous and nanocrystalline catalysts (*i.e.,* the Fe_2O_3-SC and Fe_2O_3-C series) with the nanostructured ones (*i.e.,* the Fe_2O_3-HT series). Upon deconvolution of the O 1s spectra, two surface oxygen species were detected for all the nanocrystalline samples (Figure 8c). The binding energy of *ca.* 529.3 eV, denoted as Fe-O-Fe, is characteristic of O^{2-} lattice oxygen.

However, determining the origin of the species having a binding energy of *ca.* 531.2 eV, denoted as Fe-OH, is more difficult, as this feature could either be the result of hydroxyl groups or alternatively might be due to the presence of oxygen vacancies, surface adsorbed oxygen, or carbonate species.[29] In contrast, the nanostructured catalysts presented the two peaks at *ca.* 529.3 and 531.2 eV with lower intensity, but also exhibited two additional peaks; namely a high-intensity peak centred at *ca.* 530.0 eV and a low-intensity feature centred at *ca.* 532.3 eV. These new features also correlated with the fact that these samples showed a peak at 101.7 eV in the Si 2p spectral area (see Figure 8d). Combining both pieces of XPS evidence and the results found by STEM-XEDS, the presence of a mixed phase of Si and Fe oxides can be confirmed in these samples, which arises due to the incomplete removal of the silica template during the preparation of the Fe_2O_3-HT support.

The reducibility of the bare Fe_2O_3 supports and the corresponding gold-loaded catalysts was studied by means of H_2-temperature programmed reduction (Figure 9). Similarly shaped profiles were attained for all samples, although reduction occurred at a range of different temperatures (Table 3). Comparable total hydrogen consumption values were measured, which were close to the theoretically expected value (*ca.* 19 mmol g^{-1}) for the reduction of Fe_2O_3 to Fe. A first reduction feature of medium intensity was observed with the maximum at 250-350 ºC, and a second intense broad feature at 450-650 ºC. These profiles were related to the following respective transitions $Fe_2O_3 \rightarrow Fe_3O_4$ and $Fe_3O_4 \rightarrow FeO \rightarrow Fe$, according to literature data[30], [31].

No characteristic reduction features related to gold species were observed. This result is fully consistent with the observation of gold in the metallic state from XPS characterisation. Considering the reducibility of the iron oxide supports alone, it has been proposed that the formation of nanocrystalline bridges between the iron oxide nanoparticles, such as those formed in materials prepared by nanocasting, have an influence on the reducibility of the iron species.[19] Thus, the Fe_2O_3-HT support showed a TPR profile which was clearly shifted to a higher temperature, with a low-temperature peak maximum at 447 ºC, compared to the Fe_2O_3-SC and Fe_2O_3-C supports, which displayed peaks at 319 ºC and 298 ºC, respectively. It is also highly plausible that the low reducibility of the nanostructured iron oxide might also be associated with the presence of a mixed phase of Si and Fe oxides on the nanostructured support, as observed by XEDS and XPS analysis.

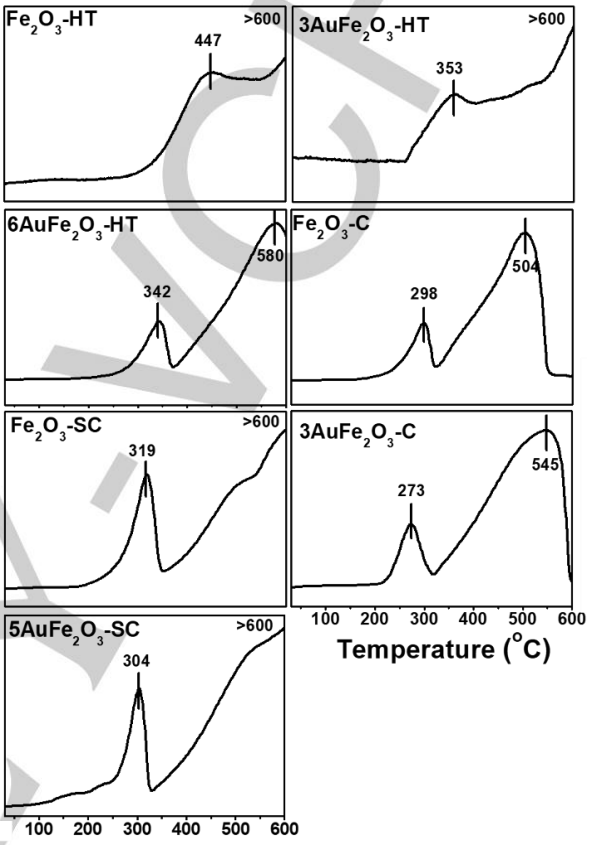

Figure 9. Hydrogen temperature programmed reduction (TPR) profiles of the various iron oxide supports and the corresponding gold loaded Fe_2O_3 catalysts.

After depositing gold nanoparticles onto the nanostructured support, 3AuFe$_2$O$_3$-HT and 6AuFe$_2$O$_3$-HT catalysts showed a significant shift in the low-temperature reduction maxima, which were observed to decrease to 353 ºC and 342 ºC, respectively. Additionally, the high-temperature maximum decreased from > 600 ºC to 580 ºC in the case of the catalyst with the highest gold loading. These results suggest that the presence of gold metallic nanoparticles, partially confined in the internal support mesoporosity, notably promoted the reduction of Fe_2O_3, despite the presence of both the nanocrystalline bridges and the mixed phase of Si and Fe oxides. In line with this, Mao *et al.* [23] have recently postulated that the partial confinement of Pt nanoparticles within the mesopores of microscale CeO_2, leads to a significant enhancement in the activity of the surface lattice oxygen of CeO_2 at the interface between Pt nanoparticles and the CeO_2 support. In the present study, we also observe a modification of the lattice oxygen species from the interaction between confined metallic Au nanoparticles and the support and it could be assumed that these lattice oxygen species could be

responsible for increasing the catalytic activity for propane total oxidation.

With respect to gold deposition on the more conventional Fe_2O_3-SC and Fe_2O_3-C supports, TPR profiles showed that the lowest temperature reduction peak was shifted to a lower temperature, *i.e.,* 304 °C and 273 °C respectively, whereas the highest temperature peak moved to marginally higher temperatures. Hence, it is evident that supporting gold nanoparticles on just the external surface of the iron oxide structures did not significantly modify the reduction characteristics of the supports, since both iron oxides displayed comparable hydrogen reduction profiles with and without the presence of gold, which is in agreement with data from other studies.[32] Therefore, it can be determined that gold deposited on the external surface of nanocrystalline α-Fe_2O_3 results in a weaker metal-support interaction as the redox properties of these latter iron oxide supports were not strongly modified by gold addition.

Table 3. Summary of temperature programmed reduction (TPR) and X-ray photoelectron spectroscopy (XPS) results for the various iron oxide supports and corresponding Au/Fe_2O_3 catalysts. The Si 2p peak corresponding to a SiO_2 pure silica film occurs at a binding energy of 102.6 eV.

	H_2-TPR	Fe 2p	Si 2p	O 1s	Au 4f	Si/Fe
	T_{max} (ºC)	BE (eV)	BE (eV)	BE (eV)	BE (eV)	
Fe_2O_3-HT	447, >600	710.9	101.6	529.9	-	1
3AuFe_2O_3-HT	353, >600	710.8	101.8	529.9	83.5	1
6AuFe_2O_3-HT	342, 580	710.9	101.5	530.0	83.8	1
Fe_2O_3-SC	319, >600	710.5	-	529.5	-	-
5AuFe_2O_3-SC	304, >600	710.4	-	529.5	83.0	-
Fe_2O_3-C	298, 504	710.2	-	529.3	-	-
3AuFe_2O_3-C	273, 545	710.4	-	529.4	83.3	-

The differences observed confirm the crucial role of internal porosity in nanostructured supports [33], which facilitates a more intimate contact between partially confined metal nanoparticles and the support.

Finally, although gold supported on nanocasted iron oxide catalysts has shown an outstanding stability under cyclic operation, see Figure 2A, the characterization of the used 6AuFe_2O_3-HT sample by different complementary techniques was carried out. As expected, no significant differences were appreciated, either in its structural characteristics (N_2 adsorption and XRD) or in its chemical surface (XPS). These results are included as supporting information (Figures S3 to S5).

DFT studies: The role of support surface structure on the availability of lattice oxygen at the metal-support interface.

The Au supported on iron oxide catalysts were modelled by placing a Au_{10} nanoparticle onto a 4-layered slab (Fe–O_3–Fe) built with a *p*(3×3) supercell of the (0001) surface, which we denote as Au_{10}/α-Fe_2O_3(0001). The Au_{10} particle had an initial geometry taken from the f.c.c. bulk lattice structure with a Au(7,3) two-layer structure. HRTEM has been used to show that Au_{10} particles present in active Au/FeO_x catalysts are bilayer in nature.[18] The bottom two slab layers (Fe–O_3–Fe) were fixed during optimization to represent the bulk lattice beneath the surface. After optimisation of the clean stoichiometric slab and Au_{10} cluster, the cluster retained its bi-layer character although movement of the Au atoms did occur.

To represent the less well-ordered surfaces expected for α-Fe_2O_3 obtained from our nanocasting synthesis, the optimised Au_{10}/α-Fe_2O_3(0001) structure was further modified by the introduction of surface grooves. These grooves were produced by the removal of stoichiometric sets of atoms from the iron oxide surface near to the Au_{10} cluster as shown in Figure 10.

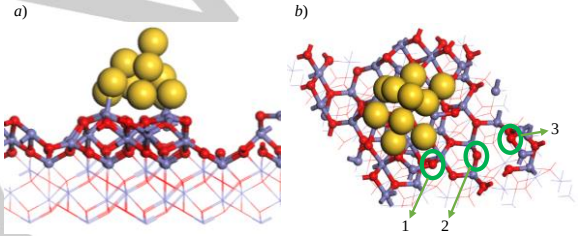

Figure 10. a) Slab model of the Au_{10} cluster on a roughened surface of α-Fe_2O_3, viewed down the [110] direction. Atoms that are fixed during optimisation are shown in line drawing mode, relaxed Fe and O atoms as ball and stick models and Au atoms in 0.7 CPK representations. b) Plan view ([0001] direction) with the positions used for oxygen defect creation indicated. Line representation is used for all lower layer atoms for clarity. *Atom colours*: Fe - blue, O – red and Au – yellow.

We have investigated different positions in the surface layer of the α-Fe_2O_3(0001) support for the creation of surface oxygen vacancies. The aim is to examine the effect of the presence of the metal nanoparticle on the removal of nearby surface oxygen. For both the Au_{10}/α-Fe_2O_3(0001) and oxidised cluster $Au_{10}O_6$/α-Fe_2O_3(0001), calculations were carried out for oxygen positions under the nanoparticle, at the interface between the particle and oxide (nearest), and at oxygen sites next nearest to the Au_{10} nanoparticle with the whole system optimised in each case. For the grooved surface, we removed 2 co-ordinate surface oxygen anions to create the oxygen defects, the sites used are shown in Figure 10b. In all cases, the single oxygen vacancy formation energy was calculated as follows:

$$E_{vac} = E(Au_{10}/Fe_{72}O_{107}) - E(Au_{10}/Fe_{71}O_{108}) – 1/2E(O_2) \quad (1)$$

where ($Au_{10}/Fe_{72}O_{107}$) denotes the oxygen defect system, ($Au_{10}/Fe_{71}O_{108}$) is the stoichiometric system, and (O_2) is the gas phase oxygen in the triplet ground state. For the oxidised cluster, $Au_{10}O_6$ should replace Au_{10} in equation (1). The vacancy creation energy defined in equation (1) gives a positive value for an endothermic process. Table 4 summarises the calculated defect

energies for the flat α-Fe_2O_3(0001) and grooved grv-α-Fe_2O_3 surfaces with and without the inclusion of a Au_{10} cluster. For the α-Fe_2O_3(0001) surface all oxygen atoms are three co-ordinate and we find a defect energy of 3.02 eV which is lowered to 2.13 eV when the defect is created near to a surface Au cluster. This is in agreement with our earlier work,[34] where we showed that this is partly due to the polarisable nature of the Au_{10} cluster which stabilises the change in oxidation state of surface Fe cations on the removal of an oxygen anion and partly due to charge transfer to the Au_{10} cluster itself. A similar effect has also been found in calculations for Au supported on other oxide surfaces, for example Au/TiO_2.[35] For the grooved surface, several different types of surface O are present. We have concentrated on two co-ordinate oxygen anions as these give rise to low defect creation energies. Introducing surface roughness into the model by adding these groove features has a very strong influence on the defect creation energy, with values between 1.00 and 1.82 eV, being calculated for the removal of two co-ordinate surface O anions at the positions indicated in Figure 10b. This is up to 1.13 eV lower than the Au_{10} decorated α-Fe_2O_3(0001) indicating that the change in the surface structure of the oxide which could be brought about by choice of synthesis method will have an important influence on the availability of lattice oxygen. Interestingly, the addition of a Au_{10} cluster to the surface to give the Au/grv-α-Fe_2O_3 models now has a relatively minor effect on the defect creation energy, even for defects quite close to the Au_{10} cluster (this can be seen by comparing grv-α-Fe_2O_3-1 and Au/grv-α-Fe_2O_3-1 in Table 4).

As discussed earlier, our STEM-XEDS and XPS measurements suggest that there is also a significant level of Si in the surface layer of the nanocast materials. One possibility is that the silica used in the casting process forms a mixed oxide phase with Fe_2O_3. As a model of such a mixed phase we have also considered the olivine structure, Fe_2SiO_4.[36, 37] The olivine unit cell was optimised using a similar DFT approach to that described for α-Fe_2O_3. A cell expansion using a cell with stoichiometry $Fe_8Si_4O_{16}$ showed an energy minimum just 1.3 % higher in volume than the experimental reference (*a* =10.607, *b* = 6.164, *c* = 4.870 *cf a* =10.460, *b* = 6.082, *c* = 4.815 (CSD: 9007046)). The most stable surface facet is indexed (100) in this setting for which we obtain a surface energy of 0.86 J m^{-2}, which in reasonable agreement with earlier DFT studies of this material.[38]

Table 4. Calculated defect formation energies for Fe_2O_3 and Au/Fe_2O_3 DFT models.

System	Defect Energy (eV)	System	Defect Energy (eV)
α-Fe_2O_3(0001)	3.02	**Au/α-Fe_2O_3(0001)**	2.13
grv-α-Fe_2O_3 – 1	1.00	**Au/grv-α-Fe_2O_3 - 1**	1.21
grv-α-Fe_2O_3 – 2	1.50	**Au/grv-α-Fe_2O_3 – 2**	1.21
grv-α-Fe_2O_3 – 3	1.82	**Au/grv-α-Fe_2O_3 – 3**	1.57

Olivine only contains Fe in the 2+ oxidation state. This means that it is unlikely that oxygen can easily be removed from the lattice as the accompanying reduction of cations cannot take place. However, the surface structure provides us with a model for how a silicon containing layer would interface with the predominant Fe_2O_3 material in the nanocast catalysts. To examine the effect of this interface we took a single FeO_6 octahedral centre from the optimised α-Fe_2O_3 structure and overlayed it on the olivine (100) surface. The octahedral FeO_6 structure was overlayed so that 3 oxygens on the surface matched closely with the O atoms of the FeO_6 fragment and then the remaining three O atoms where replaced with hydroxyl groups (Figure S6*a*). The three O atoms in the octahedral fragment could be matched within 0.25 Å of the surface O atom positions. These three fragment O atoms were then deleted to provide a model of the interface of the silicon-rich olivine surface and an Fe(3+) centre. The slab model was then re-optimised and the resulting structure can be seen in Figure S6*b*). On optimisation the Fe(3+) has moved away from two of the surface O ions and the FeO_6 structure has rotated to bring two of the OH groups into bridging positions with surface Fe(2+) ions. This results in a loss of the octahedral symmetry that the Fe(3+) ion would have in α-Fe_2O_3 and suggests that the interface between an olivine like iron silicate and α-Fe_2O_3 would be quite strained, which would be expected to change the availability of lattice oxygen.

Comments on the activity of gold-loaded Fe_2O_3 catalysts.

The explanation for differences in the catalytic activity for propane total oxidation of the various materials studied here is based on several parameters. For the bare iron oxide support without gold nanoparticles, the surface area was not a sufficient descriptor to explain the total oxidation of propane, as previously reported.[19] Indeed, both the Fe_2O_3-SC and Fe_2O_3-C materials show higher catalytic activity for propane oxidation than the nanostructured Fe_2O_3-HT support, which presents a markedly higher surface area. As observed by H_2-TPR, the nanostructured Fe_2O_3-HT support showed a lower reducibility than both nanocrystalline Fe_2O_3-C and mesoporous Fe_2O_3-SC supports. This behaviour might be related to the presence of crystalline bridges between adjacent iron oxide nanoparticles, which themselves were partially covered by a mixed phase of Si and Fe oxides, stabilizing the catalyst surface and leading to the formation of iron species that were more difficult to reduce. The specific nature of the active sites responsible for the total oxidation of propane in metal oxides is not completely understood; however, the catalytic activity displayed during the deep oxidation of light alkanes, such as propane, is closely related to the ease of reduction and re-oxidation of the active sites in the catalyst. Hence, many studies have demonstrated that alkane oxidation on metal oxides takes place via a Mars-van Krevelen mechanism involving lattice oxygen through a redox cycle.[39]-[42] Accordingly, for the total oxidation of propane we have previously established a clear correlation between reducibility (quantified as the temperature of the maximum of the first reduction feature) and catalytic activity (normalized per unit surface area) for different Fe_2O_3 catalysts. This suggests that the rate limiting step for propane oxidation over iron oxides is the reduction step and that the oxidation proceeds utilising bulk lattice oxygen through a Mars-van Krevelen mechanism, as we have also observed in our current study. However, this same trend is not fully observed when iron oxide catalysts loaded with gold nanoparticles are considered, as

shown in Table 1. Whilst a higher specific activity is observed for the gold-loaded catalysts on the nanostructured Fe_2O_3-HT support as compared to the bare support, which is in accordance with its improved reducibility, the opposite effect is true when gold-nanoparticles are supported on Fe_2O_3-SC and Fe_2O_3-C supports, despite the fact that their reducibility was slightly increased. Therefore, it can be postulated that the improved redox properties of gold-loaded iron oxide nanostructures is not the sole parameter controlling its catalytic performance for VOC removal.

The reaction mechanism for gold nanoparticle catalysts deposited on reducible supports is more complex, as gold plays a key role promoting both adsorption of VOCs and oxygen activation. It is generally accepted that the rate of reaction is dictated by the dissociation of O_2 to yield atomic oxygen at the oxygen vacancies near the metal–support interface. This step is relatively slow in gold-based systems[43],[44] due to the high activation barrier of ~2.2 eV.[43] However, for the gold sitting on a porous iron oxide support, we have calculated that the presence of surface roughness on the oxide support can significantly decrease this value to ~1.2 eV when a Au_{10} cluster is located near the surface corrugation. This theoretical scenario might be increasingly important when gold nanoparticles are deposited on nanostructured supports prepared by nanocasting. As shown previously, micropores intersecting the Fe_2O_3-HT surface seem to act as anchoring points for small gold nanoparticles at the inner mesoporosity of the nanostructured support, which could facilitate oxygen activation at the metal-support interface according to DFT calculations. In addition, it is worth commenting that although the Fe_2O_3-SC support is also a mesoporous support, there is neither any intra-particle mesoporosity, nor surface porosity, which could be equated to surface roughness. Therefore, gold is only deposited on the inter-particle external surfaces in Fe_2O_3-SC-type supports, limiting the extent to which oxygen activation can occur at the metal-support interface. Indeed, gold deposition on the Fe_2O_3-SC support seems to be blocking the iron oxide active sites, since the specific activity of the 5Au Fe_2O_3-SC catalyst was decreased compared to the bare Fe_2O_3-SC material, despite improved redox properties. The same is shown to be true for the gold catalyst supported on the nanocrystalline iron oxide denoted Fe_2O_3-C.

As inferred from N_2 adsorption and TEM measurements, the deposition of gold nanoparticles on the Fe_2O_3-HT support, obtained by the hard-templating route, leads to a partial confinement of small gold nanoparticles into the intra-particle mesoporosity of the support. According to the work of Behm and co-workers, who studied Au/TiO_2 catalysts,[45] the quantity of removable oxygen was essentially correlated with the number of perimeter sites between gold nanoparticles and the support, showing a linear relationship. Smaller gold nanoparticles have a greater quantity of perimeter sites when normalised for gold content, and thus gold particle size effects can lead to increased redox activity. In spite of the absence of a relevant amount of large gold particles in Au/Fe_2O_3-HT catalysts, which certainly appears in the other gold-based iron oxide catalysts, gold particle size is not believed to be the only effect responsible for the enhanced activity, since both gold-based iron oxide catalyst shows comparable gold particle size distribution. The nanostructured nature of the support is also thought to have an important influence on the number of gold-support perimeter sites. This parameter could also be increased by the presence of Au nanoparticles being in contact with more than one Fe_2O_3 particle simultaneously – *i.e.,* creating two or more planar interfaces (and thus more periphery line length) per Au particle. Superior metal-support contact area could be attained for the mesoporous nanostructured support compared to the gold nanoparticles supported on the external surface of nanocrystalline Fe_2O_3-C, or in the inter-particle mesoporosity of Fe_2O_3-SC. Hence, the enhanced activity achieved with the gold-based Fe_2O_3-HT catalyst could also be associated with an increased amount of perimeter sites at the metal-support interface, controlled by support nanostructure, where oxygen can be more easily activated due to the presence of a roughened (microporosity), leading to an overall enhancement of activity.[46]

Finally, it has been observed that the surface of the Fe_2O_3-HT support is covered by a mixed phase of Si and Fe oxides, where gold nanoparticles are deposited. This is not the situation for the other iron oxide supports studied, as they do not contain the silicon. As a comparable model of the mixed Si-Fe oxide phase, DFT simulation studies have suggested that the interface between an olivine -like iron silicate and α-Fe_2O_3 is quite strained, most likely improving the availability of surface lattice oxygen. Therefore, the deposition of gold nanoparticles over this mixed Si-Fe oxide phase, where oxygen can be more easily activated at the gold-support interphase, might be another key parameter in the better performance observed for the nanostructured catalysts. This promoting effect is quite surprising and further studies are needed to confirm the key role of this type of mixed surface phase over surface oxygen activation, since silica-type materials are not usually considered as an adequate matrix for gold-based catalysts. Silica supports tend to enlarge gold particles deposited over its surface due to the presence of weak Au–support interactions. Additionally, gold on silica cannot readily form activated oxygen species and consequently the C-H bond cleavage of propane demands more severe conditions.

Summarising, it can be tentatively proposed that propane total oxidation on gold nanoparticles confined into a nanostructured Fe_2O_3 catalyst followed an Au-assisted Mars-van Krevelen mechanism, in which propane is adsorbed onto the catalyst surface and reacts with active oxygen species created in the vicinity of the metal-support interfacial region. The presence of a porous nanostructure in the Fe_2O_3-HT support has several positive effects: i) a stronger metal-support interaction facilitating oxygen activation at the interface due to the presence of confined small gold nanoparticles, which are stabilised due to the nanostructured nature of the support (microporosity and mesoporosity); ii) a higher contact surface area between the partially confined metal nanoparticles and the support; iii) a more reducible support due to the formation of more active surface lattice oxygen, and iv) a higher defect concentration and consequently a better availability of lattice oxygen due to both the surface microporosity of the support and the presence of a mixed Si-Fe oxide phase.

Table 5. Total oxidation of propane on catalysts containing iron

Catalysts	$[C_3H_8]$ /ppm	GHSV /h^{-1}	T10	T50	T90
Fe_2O_3[19]	8000	20000	375	>425	
Fe_2O_3 hard template[19]	8000	20000	265	315	370
Fe_2O_3[16]	15000	[b]	~ 450		
MnOx-FeOx[16]	15000	[b]	~ 320		
Clay honeycomb monolith 11%Fe_2O_3[48]	10000	2300	359	420	473
LaCaFeOx perovskite[49]	10000	20000	325	375	400
$ZnFe_2O_4$[50]	2000	13000	362	384	400
Pt/$ZnFe_2O_4$[50]	2000	13000	217	228	238
PdCeFe[51]	5000	15000	210	325	370
Au/FeOx[52]	71000	3600	300		
Fe_2O_3 nanocasting[a]	8000	100000	317	370	418
Au/Fe_2O_3 nanocasting[a]	8000	100000	268	334	370

[a] This work.

[b] 3 m^2 of exposed area of catalyst and 300 ml/min

Finally, the activity of the most active catalyst shown in this work was benchmarked versus other iron-based catalysts reported in the literature in Table 5. 6AuFe_2O_3-HT displays a remarkable high reactivity, although those containing Pd or Pt show better performance.

Conclusions

The addition of gold by a deposition-precipitation method to iron oxide prepared using a hard template has led to a substantial enhancement in the total oxidation of propane. This positive effect of gold does not take place if other iron oxides are used as supports. The enhanced behaviour of gold catalysts supported on nanocast Fe_2O_3 is mainly related to the porous nanostructure of the support. In these catalysts a stronger metal-support interaction takes place, facilitating oxygen activation at the interface. DFT studies have concluded that formation of defects are more favourable and there is better availability of lattice oxygen in the Au/Fe_2O_3-HT catalysts which is related to both the surface roughness of the support and the formation of a Si-Fe mixed oxide phase. The presence of small gold nanoparticles, which are stabilised due to the nanostructured nature of the support (microporosity and mesoporosity), also plays an important role in the enhanced reactivity.

Experimental Section

Synthesis of materials.

An ordered mesoporous Fe_2O_3 catalyst was prepared in an open vessel following a hard templating nanocasting route[47] using a silica KIT-6 template. The Fe_2O_3 obtained by this method was denoted Fe_2O_3-HT, and subsequently gold was deposited onto this material by a deposition-precipitation process, with target gold loadings of 3 and 6 wt %, giving catalysts denoted as 3AuFe_2O_3-HT and 6AuFe_2O_3-HT respectively.

For comparative purposes, two iron oxides with different characteristics were also employed as supports for gold. A mesoporous support formed by aggregation of iron oxide nanocrystals was prepared using aqueous iron nitrate with oxalic acid added as a swelling agent (molar ratio = 1:5). The solution was heated at 80 °C until most of the water had evaporated. The solid was dried for 16 h at 120 °C and then calcined in static air in two steps; 2 h at 300 °C and then 2 h at 500 °C.[18] The iron oxide obtained with this method was named Fe_2O_3-SC and subsequently, gold was deposited by deposition-precipitation, with a target gold loading of 5 wt %, yielding a catalyst denoted as 5Au Fe_2O_3-SC.

Finally, a nanocrystalline Fe_2O_3 was also synthesized by dissolving iron (II) nitrate (Fluka, purity > 98%) in deionised water. This solution was evaporated to dryness, and then dried for 16 h at 120 ºC, and finally calcined in static air at 500 ºC for 4 h.[18] The iron oxide obtained with this method was named Fe_2O_3-C and subsequently, gold was deposited by deposition-precipitation, with a target gold loading of 3 wt %, giving a catalyst denoted as 3AuFe_2O_3-C.

Characterization of materials.

The KIT-6 template, Fe_2O_3 supports and catalyst samples were characterized by N_2 adsorption at -196 ºC, using a Micromeritics ASAP 2020 apparatus. Samples were degassed at 150 ºC prior to analysis. From these data, the following textural parameters were calculated. Multi-point Brunauer–Emmet–Teller (BET) surface area (S_{BET}) was estimated over the relative pressure range from 0.05 to 0.25. The total pore volume (V_T) was calculated using the adsorbed volume at a relative pressure of 0.95. The pore size distribution and mean pore size (d_0) of the mesoporous materials were analysed using the Barrett–Joyner–Halenda (BJH) and the NL-DFT methods applied to the adsorption branch of the isotherm and assuming cylindrical pore geometry.

Powder X-ray diffraction (XRD) was used to identify the crystalline phases present in the samples. A Bruker D8 Advance diffractometer with a monochromatic Cu K_α X-ray source operated at 40 kV and 40 mA was employed. The experimental patterns were calibrated against a silicon standard and the crystalline phases were identified by matching the experimental patterns to the JCPDS powder diffraction file database.

X-ray photoelectron spectroscopy (XPS) measurements were made on a Kratos Axis ultra DLD photoelectron spectrometer using a non-monochromatized Mg K_α X-ray source (hv = 1253.6 eV). An analyser pass energy of 50 eV was used for survey scans and 20 eV for detailed scans. Binding energies were referenced to the C1s peak from adventitious carbonaceous species, assumed to have a binding energy of 284.8 eV. XPS data were analysed using CasaXPS software. A Gaussian–Lorentzian shape function was used to peak fit the corrected spectra. Iterations were performed using the Marquardt method. Relative standard deviations were always lower than 1.5%.

Morphological and structural characterization of the sample was performed by transmission electron microscopy (TEM) by using an FEI Tecnai G^2 F20 microscope equipped with a FEG source and operated at 200 kV. The samples were prepared by sonication in absolute ethanol for a few minutes, and a drop of the resulting suspension was deposited onto a holey-carbon film supported on a copper grid, which was subsequently dried. Higher resolution imaging experiments were carried out on dry dispersed samples in an aberration corrected JEOL ARM 200CF scanning transmission electron microscope (STEM) operated at 200kV. This

instrument was equipped with a Centurio silicon drift detector for X-ray Energy Dispersive Spectroscopy (XEDS) analysis.

Temperature programmed reduction (TPR) analyses were carried out in a Micromeritics Autochem 2920 instrument equipped with a thermal conductivity detector, operated under a 50 mL min^{-1} 10% H_2/Ar flow at temperatures between -50 and 800 °C, with a heating rate of 10 °C min^{-1}.

DFT calculations were performed using the density functional theory plane wave basis set code VASP, (Vienna ab-initio simulation package).[53]-[56] A plane wave cut-off of 500 eV was employed. The iron atom 3*d*, 4*s*, oxygen 2*s*, 2*p*, and gold 5*d*, 6*s* electrons were treated explicitly as valence electrons and the projector augmented wave (PAW) method was used to represent the remaining core states of all atoms.[57],[58] The Perdew-Burke-Ernzerhof (PBE) functional was used throughout this work.[59],[60] An on-site Coulomb interaction correction (PBE+U) following Dudarev's approach (U_{eff}=U – J) was applied to describe the strongly correlated *d*-states of iron.[61] We have applied a U_{eff} of 4.0 eV. The Fe^{3+} ions in the weak field of the oxide lattice have a formal d^5 configuration. The magnetic moment of ±5 in the sequence **+ – – + + – – +** for the iron layers in the direction perpendicular to the surface plane were used throughout this work. Tests with alternative ordering patterns confirmed that this gives an optimised structure with the lowest energy magnetic moment arrangement. These parameters were set based on our previous work in which we have shown good agreement with experimental data for the lattice parameters, bulk moduli, the density of states, band gap, and Fe site magnetic moment for the α-Fe_2O_3 system.[34],[62] To accommodate the gold nanoparticle, a vacuum gap of 25 Å perpendicular to the surface of the α-Fe_2O_3(0001) slab was introduced. The large surface area of the slab allows structural optimisations to be carried out at the Γ-point. A dipole correction along the *z*-direction of the slab was applied in all calculations.

Catalytic testing.

The propane oxidation activity of the catalysts was measured using a fixed-bed laboratory microreactor. For each experiment, 100 mg of powdered catalyst was placed in a 1/2inch o.d. quartz reactor tube. The reactor feed contained 8000 ppm propane in air, with a flow rate to achieve a gas hourly space velocity (GHSV) of 100,000 h^{-1}. Reactants and products were analysed by an on-line gas chromatograph fitted with a thermal conductivity and a flame ionization detector. Two chromatographic columns were employed: (i) Porapak Q (for CO_2 and hydrocarbons) and (ii) Molecular Sieve 5A (to separate CO, O_2 and N_2). The difference between the inlet and outlet concentrations was used to calculate conversion data. In order to corroborate these data, the chromatographic area of CO_2 was used as the comparative reference. Measured carbon balances were always 100 ± 2%. Blank experiments were conducted in an empty reactor, which showed negligible activity over the temperature range used in this study.

Acknowledgements

T. García would like to acknowledge the Spanish Ministry of Education, Culture and Sports through its Mobility program for stays of senior researchers and professors in foreign countries (MECD, grant number PRX15/00144) for funding. Computational facilities supplied by Wales' national supercomputing service provider, High-Performance Computing (HPC) Wales, are gratefully acknowledged. Via our membership of the UK's HPC Materials Chemistry Consortium, which is funded by EPSRC (EP/L000202), this work made use of the facilities of HECToR and ARCHER, the UK's national high-performance computing service, which is funded by the Office of Science and Technology through EPSRC's High End Computing Programme. CJK gratefully acknowledges funding from the National Science Foundation Major Research Instrumentation program (GR# MRI/DMR-1040229). Authors from UV thank the University of Valencia (UV-INV-AE16-484416 project) and MINECO (MAT2017-84118-C2-1-R project) for funding.

Keywords: nanocasting • mesoporous α-Fe_2O_3 • catalytic total oxidation • propane • gold

[1] A. Corma, H. Garcia, *Chem. Soc. Rev.* **2008**, *37*, 2096-2126.
[2] S. Scirè, L.F. Liotta, *Appl. Catal. B.* **2012**, *125*, 222-246.
[3] R.D. Waters, J.J. Weimer, J.E. Smith, *Catal. Letters* **1995**, *30*, 181-188.
[4] F. Ying, S. Wang, C-T. Au, S-Y Lai, *Gold Bull.* **2010**, *43*, 241-251.
[5] L. Delannoy, K. Fajerwerg, P. Lakshmanan, C. Potvin, C. Methivier, C. Louis, *Appl. Catal. B.* **2010**, *94*, 117-124.
[6] P. Lakshmanan, L. Delannoy, V. Richard, C Methivier, C Potvin, C. Louis, *Appl. Catal. B.* **2010**, *96*, 117-125.
[7] D. Andreeva, P. Petrova, J.W. Sobczak, L. Ilieva, M. Abrashev, *Appl. Catal. B.* **2006**, *67*, 237-245.
[8] G.C. Bond, D.T. Thompson, *Gold Bull.* **2000**, *33*, 41-50.
[9] B. Liu, C, Li, Y. Zhang, Y. Liu, W. Hu, Q. Wang, L. Han, J. Zhang, *Appl. Catal. B.* **2012**, *111–112*, 467-475.
[10] J. Zhang, Y. Jin, C. Li, Y. Shen, L. Han, Z. Hu, X. Di, Z. Liu, *Appl. Catal. B.* **2009**, *91*, 11-20.
[11] T. García, B. Solsona, S.H. Taylor, in *Handbook of advanced methods and processes in oxidation catalysis*, Imperial College Press: UK. **2014**, pp. 51-90.
[12] B.E. Solsona, T. García, C.D. Jones, S.H. Taylor, A.F. Carley, G.J. Hutchings, *Appl. Catal. A.* **2006**, *312*, 67-76.
[13] T.V. Choudhary, S. Banerjee, V.R. Choudhary, *Appl. Catal. A.* **2002**, *234*, 1-23.
[14] S. Minicò, S. Scirè, C. Crisafulli, R. Maggiore, S. Galvagno, *Appl. Catal. B.* **2000**, *28*, 245-251.
[15] S. Scirè, S. Minicò, C. Crisafulli, S. Galvagno, *Catal. Comm.* **2001**, *2*, 229-232.
[16] M. Baldi, V. Sánchez-Escribano, J.M. Gallardo Amores, F. Milella, G. Busca, *Appl. Catal. B* **1998**, *17***,** 175-182.
[17] F.G. Duran, B.P. Barbero, L.E. Cadus, C. Rojas, M.A. Centeno, J.A. Odriozola, *Appl. Catal. B* **2009**, *92*, 194-201.
[18] Y. Xia, H. Dai, H. Jiang, L. Zhang, J. Deng, Y. Liu, *J. Hazard. Mater.* **2011**, *186*, 84-91.
[19] B. Solsona, T. García, R. Sanchis, M.D. Soriano, M. Moreno, E. Rodríguez-Castellón, S. Agouram, A. Dejoz, J.M. López Nieto, *Chem. Eng. J.* **2016**, *290*, 273-281.
[20] Y. Zhang, J. Deng, L. Zhang, H. Dai, *Chin. Sci. Bull.* **2014**, *59*, 3993-4002.
[21] S. Carabineiro, N. Bogdanchikova, P.B. Tavares, J.L. Figueiredo, *RSC Adv.* **2012**, *2***,** 2957-2965.
[22] Z. Zhong, J. Ho, J. Teo, S. Shen, A. Gedanken, *Chem. Mater.* **2007**, *19***,** 4776-4782.
[23] M. Mao, H. Lv, Y. Li, Y. Yang, M. Zeng, N. Li, X. Zhao, *ACS Catal.* **2016**, *6*, 418-427.
[24] F. Kleitz, S.H. Choi, R. Ryoo, *Chem. Comm.* **2003**, *39*, 2136-2137.
[25] Y. Ren, Z. Ma, R.E. Morris, Z. Liu, F. Jiao, S. Dai, P.G. Bruce, *Nat. Comm.* **2013**, *4*, 2015.
[26] K. Zhao, H. Tang, B. Qiao, L. Li, J. Wang, *ACS Catal.* **2015**, *5*, 3528-3539.
[27] S. Minicò, S. Scirè, C. Crisafulli, S. Galvagno, *Appl. Catal. B* **2001**, *34*, 277-285.

[28] A.P. Grosvenor, B.A. Kobe, M.C. Biesinger, N.S. McIntyr, *Surf. Interface Anal.* **2004**, *36*, 1564-1574.
[29] A.M. Venezia, G. Pantaleo, A. Longo, G. Di Carlo, M.P. Casaletto, F.L. Liotta, G. Deganello, *J. Phys. Chem. B* **2005**, *109*, 2821-2827.
[30] K. Park, J.H. Jung, H. Seo, O. Kwon, *Microp. Mesop.Mat.* **2009**, *121*, 219-225.
[31] F.G.E. Nogueira, J.H. Lopes, A.C. Silva, R.M. Lago, J.D. Fabris, L.C.A. Oliveira, *Appl. Clay Sci.* **2011**, *51*, 385-389.
[32] M.A. Soria, P. Pérez, S.A.C Carabineiro, F.J. Maldonado-Hódar, A. Mendes, L.M. Madeira, *Appl. Catal. A* **2014**, *470*, 45-55.
[33] H. Tang, Y. Zeng, D. Liu, D. Qu, J. Luo, K. Binnemans, D.E. De Vos, J. Fransaer, D. Qu, S-G. Sun, *Nano Energy* **2016**, *26*, 131-138.
[34] K.L. Howard, D.J. Willock, *Faraday Disc.* **2011**, *152*, 135-151.
[35] P. Schlexer, D. Widmann, R. J. Behm, G. Pacchioni, *ACS Catal.* **2018**, *8(7)*, 6513-6525.
[36] G. Nover, G. Will, *Z. Kristallogr.* **1981**, *155*, 27-45.
[37] O. Ballet, H. Fuess, T. Friezche, *Phys. Chem. Minerals* **1987**, *15*, 54-58.
[38] C.A. Downing, B Ahmady, C.R.A. Catlow, N.H. de Leeuw, *Phil Trans R Soc A* **2013**, *371*, 20110592.
[39] C. Li, Y. Shen, M. Jia, S. Sheng, M.O. Adebajo, H Zhu, *Catal. Commun.* **2008**, *9*, 355-361.
[40] N. Bahlawaue, *Appl. Catal. B* **2006**, *67*, 168-176.
[41] B. Solsona, T.E. Davies, T. García, I. Vázquez, A. Dejoz, H. Taylor, *Appl. Catal. B* **2008**, *84*, 176-184.
[42] B. Solsona, M. Pérez-Cabero, I. Vázquez, A. Dejoz, T. García, J. Álvarez-Rodríguez, J. El-Haskouri, D. Beltrán, P. Amorós, *Chem. Eng. J.* **2012**, *187*, 391-400.
[43] X.Y. Deng, B.K. Min, A. Guloy, C.M. Friend, *J. Am. Chem. Soc.* **2005**, *127*, 9267-9270.
[44] Z.P. Liu, P. Hu, A. Alavi, *J. Am. Chem. Soc.* **2002**, *124*, 14770-14779.
[45] M. Kotobuki, R. Leppelt, D.A. Hansgen, D.R.J. Widmann, J. Behm, *Catal.* **2009**, *264*, 67-76.
[46] T.F. Zhang, S.M. Driver, S.J. Pratt, D.A. King, *Surf. Sci.* **2013**, *615*, 1-5.
[47] F. Jiao, A. Harrison, J.C. Jumas, A.V. Chadwick, W. Kockelmann, P.G. Bruce, *J. Am. Chem. Soc.* **2006**, *128*, 5468-5474.
[48] M. Assebban, A. El Kasmi, S. Harti, T. Chafil, *J. Hazard. Mat.* **2015,** 300, 590-597**.**
[49] B. P. Barbero, J. A. Gamboa, L. E. Cadús, *Appl. Cat. B*, **2006**, 65 (1-2), 21-30.
[50] M. Zawadzki, J. Okal. *Catal. Today*, **2015**, 257, 136-143.
[51] J.-Y. Luo, M. Meng, J.-S. Yao, X.-G. Li, Y.-Q. Zha, X. Wang, T.-Y. Zhang, *Appl. Catal. B.*, **2009**, 87 (12), 92-103.
[52] M. Gasior, B. Grzybowska, K. Samson, M. Ruszel, J. Haber, *Catal. Today,* **2004**, 91–92, 131-135.
[53] G. Kresse, J. Hafner, *Phys. Rev. B* **1993**, *47*, 558-561.
[54] G. Kresse, J. Hafner, *Phys. Rev. B* **1994**, *49*, 14251-14269.
[55] G. Kresse, J. Furthmüller, *Comp. Mater. Sci.* **1996**, *6*, 15-50.
[56] G. Kresse, J. Furthmüller, *Phys. Rev. B* **1996**, *54*, 11169-11186.
[57] P.E. Blochl, *Phys. Rev. B* **1994**, *50*, 17953-17979.
[58] G. Kresse, D. Joubert, *Phys. Rev. B* **1999**, *59*, 1758-1775.
[59] J.P. Perdew, K. Burke, M. Ernzerhof, *Phys. Rev. Lett.* **1996**, *77*, 3865-3868.
[60] J.P. Perdew, K. Burke, M. Ernzerhof, *Phys. Rev. Lett.* **1997**, *78*, 1396.
[61] S.L. Dudarev, G.A. Botton, S.Y. Savrasov, C.J. Humphreys, A.P. Sutton, *Phys. Rev. B.* **1998**, *57*, 1505-1509.
[62] S.W. Hoh, L. Thomas, G. Jones, D.J. Willock, *Research on Chemical Intermediates* **2015**, *41*, 9587-9601.

10.1002/cctc.201900210

WILEY-VCH

Entry for the Table of Contents (Please choose one layout)

Layout 1:

FULL PAPER

Confined gold particles on the nanocasted Fe_2O_3 facilitates the production of highly reactive oxygen vacancies at the metal-support interface.

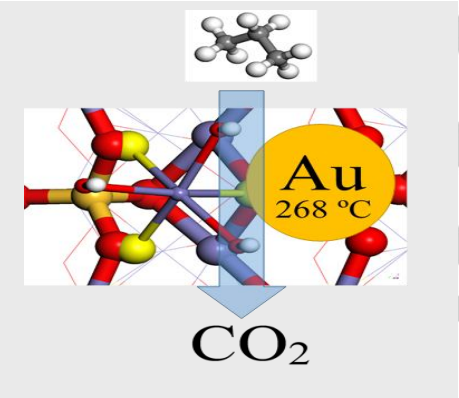

Tomás García, José M. López, Benjamín Solsona,* Rut Sanchis, David J. Willock, Thomas E. Davies, Li Lu, Qian He, Christopher J. Kiely, and Stuart H. Taylor**

Page No. – Page No.

The key role of nanocasting in gold-based Fe_2O_3 catalysts for oxygen activation at the metal-support interface